(Revision 1)

Tetrahedrite-(Ni), $Cu_6(Cu_4Ni_2)Sb_4S_{13}$, the first nickel member of tetrahedrite group mineral from Luobusa chromite deposits, Tibet, China

YANJUAN WANG[1,3], RUJUN CHEN[2], XIANGPING GU[2,*], FABRIZIO NESTOLA[3,*], ZENGQIAN HOU[1,4], ZHUSEN YANG[5], GUOCHEN DONG[1], GUO HU[6] AND KAI QU[6,7]

[1] School of Earth Sciences and Resources, China University of Geosciences (Beijing), Beijing 100083, China.
[2] School of Geosciences and Info-Physics, Central South University, Changsha 410083, Hunan, China.
[3] Department of Geosciences, University of Padova, Padova 35131, Italy.
[4] Institute of Geology, Chinese Academy of Geological Sciences, Beijing 100037, China.
[5] Institute of Mineral Resources, Chinese Academy of Geological Sciences, Beijing 100037, China
[6] Tianjin Center, China Geological Survey, Tianjin 300170, China.
[7] School of Earth Sciences and Engineering, Nanjing University, Nanjing 210023, China
*E-mail: guxp2004@163.com; fabrizio.nestola@unipd.it

ABSTRACT

Tetrahedrite-(Ni) (IMA2021-031), ideally $Cu_6(Cu_4Ni_2)Sb_4S_{13}$, is the first natural Ni-member of tetrahedrite group mineral found in Luobusa chromite deposit, Tibet, China. The new species occurs as anhedral grains 2 to 20 μm in size, associated with gersdorffite, vaesite, and chalcostibite, which are disseminated in a matrix of dolomite, magnesite, quartz, Cr-rich mica and Cr-bearing clinochlore. Tetrahedrite-(Ni) is black in colour with a reddish black streak and metallic luster. It is brittle with uneven fractures and has a calculated density of 5.073 $g \cdot cm^{-3}$. The mean values of 9 electron microprobe analyses(wt%) are: Cu 39.83, Ni 5.67, Fe 1.45, Sb 21.69, As 5.45, S 25.39, total 99.48, and the empirical formula calculated on the basis of cation = 16 *apfu* is $^{M(2)}Cu_{6.00}{}^{M(1)}[Cu_{4.03}(Ni_{1.55}Fe_{0.42})_{\Sigma 1.97}]_{\Sigma 6.00}{}^{X(3)}(Sb_{2.85}As_{1.16})_{\Sigma 4.01}S_{12.67}$. Tetrahedrite-(Ni) is cubic, with space group $I\bar{4}3m$, $a = 10.3478(4)$ Å, $V = 1108.00(14)$ Å^3, and $Z = 2$. Its crystal structure has been solved by X-ray single-crystal diffraction on the basis of 188

independent reflections, with a final $R_1 = 0.0327$. Tetrahedrite-(Ni) is isostructural with tetrahedrite group minerals. It represents the first natural tetrahedrite-group mineral with Ni-dominated charge-compensating constituent. Tetrahedrite-(Ni) may be the product of late-serpentinization at moderately high-temperature conditions around 350 °C. In this case, tetrahedrite-(Ni) and its mineral paragenesis record an entire geological process of nickel enrichment, migration, activation, precipitation, and alteration from deep mantle to shallow crust.

Keywords: Tetrahedrite-(Ni), new mineral, tetrahedrite group, crystal structure, serpentinization, listvenite, Luobusa chromitite

INTRODUCTION

Tetrahedrite-group minerals are the frequent sulfosalts in different types of ore deposits worldwide (Johnson et al. 1988), with the general formula ${}^{M(2)}A_6{}^{M(1)}(B_4C_2)^{X(3)}D_4{}^{S(1)}Y_{12}{}^{S(2)}Z$, where A = Cu^+, Ag^+, □ [vacancy], and $[Ag_6]^{4+}$ clusters; B = Cu^+, and Ag^+; C = Zn^{2+}, Fe^{2+}, Hg^{2+}, Cd^{2+}, Mn^{2+}, Cu^{2+}, Cu^+, and Fe^{3+}; D = Sb^{3+}, As^{3+}, Bi^{3+}, and Te^{4+}; Y = S^{2-} and Se^{2-}; and Z = S^{2-}, Se^{2-}, and □ (Biagioni et al. 2020a). They are considered as the most complex isotypic series among the sulfosalts, owing to the multiplicity of iso- and heterovalent substitutions (Moëlo et al. 2008). The special *M*(1) is a tetrahedrally coordinated site with a valency-imposed double site-occupancy of 2/3 B^+ and 1/3 C^{2+} cations. The different charge-compensating constituents (C constituents) are usually represented by divalent transition elements, using a hyphenated suffix between parentheses to make explicit the species belonging to these series (Biagioni et al. 2020a).

As a transition element, nickel (Z = 28) is both siderophile (i.e., associated with iron) and chalcophile (i.e., associated with sulfur). So, it seems to be easy to form nickel-rich tetrahedrite according to the substitution mechanism of equivalent elements [i.e., Fe (Z = 26), Cu (Z = 29), Zn (Z = 30)]. However, nickel end-member tetrahedrite had not been reported for more than 200 years after tennantite was discovered [now renamed to tennantite-(Fe), Biagioni et al. 2020a, the first mineral in the ancient group described by the brothers R. Phillips and W. Phillips in 1819]. Although D'Achiardi (1881) reported a Ni dominant tetrahedrite from the Frigido mine, latter studies revealed that that sample was actually an intergrowth of tetrahedrite-(Fe) and Ni-bearing minerals (Carrozzini et al. 1991). Some minor nickel-bearing tennantite-(Zn) in copper-rich *rubané* ore from the Corvo deposit was also reported by Serranti et al. (2002), but its nickel content is below 0.1%. Despite the lack of documented natural analogs, synthetic nickel tetrahedrite phase with 2 Ni (*apfu*) was studied by Makovicky and Karup-Møller (1994). In the last decade, due to the potential large-scale thermoelectric (TE) application in the field of waste heat recovery in the power-producing, processing, and automobile industries (Lu et al. 2015), the structural stability and thermoelectric properties of the synthesized Ni-bearing tetrahedrite phase have been described and discussed by Barbier et al. (2015), Lu et al. (2015), and Suekuni et al. (2013). During a systematic investigation of sulfosalts from the Luobusa chromite deposit, some mineral inclusions characterized by nickel-rich tetrahedrite phase corresponding to potential $Cu_6(Cu_4Ni_2)Sb_4S_{13}$ were found. Further chemical and crystallographic studies confirmed that it's the first natural Ni-dominance tetrahedrite group mineral, allowing the proposal of new mineral species tetrahedrite-(Ni). The new mineral and its name have been approved by the Commission on New Minerals,

Nomenclature and Classification of the International Mineralogical Association (IMA-CNMNC) (IMA2021-031, Wang et al. 2021). Type material is deposited at the Geological Museum of China, No. 16, Yangrou Hutong, Xisi, Beijing 100031, People's Republic of China, under catalogue number M16118.

In this paper, the description of tetrahedrite-(Ni) is reported and the origin of nickel, forming temperature, and geological significance of the new species are discussed.

GEOLOGICAL BACKGROUND

Tetrahedrite-(Ni) was found in the Luobusa ophiolite-hosted chromite deposit (29°10'58.0" N, 92°17'47.6" E), which is about 16 km northeast of Qusum County, Tibet, China. The Luobusa ophiolite, which hosts the largest known chromite deposit in China, is located in the eastern part of the nearly 2000 km E–W trending Indus-Yarlung Zangbo suture zone (ITSZ). The ITSZ separates the Indian Subcontinent to the south from the Lhasa Block in the north (Fig. 1a) (Nicolas et al. 1981). There are two regions, ductile to ductile–brittle thrust faults within this belt: the North Luobusa–Zedang thrust (NLZT) and the South Luobusa–Zedang thrust (SLZT) (Liang et al. 2011; Xu et al. 2015) (Fig. 1b).

The Luobusa–Kangjinla ophiolite extends about 25 km long and 2–4 km wide. From the west to the east, three districts are named Luobusa, Xiangkashan, and Kangjinla. The ophiolites include a mantle sequence, a transition zone, and a serpentinite mélange zone (Zhou et al. 1996). The mantle peridotite mainly consists of harzburgite and clinopyroxene-bearing harzburgite, with minor lherzolite and dunite. About 100-200 m of thick transition-zone dunite underlying the entire sequence occurs along the northern boundary fault, and previous pseudostratigraphy studies suggest that the ophiolite is overturned (Malpas et al.

2003). The ophiolitic mélange zone contains dismembered pillow lava, gabbro, pyroxenite, and chert blocks cropping out north of the cumulates (Xiong et al. 2015; Yang et al. 2004). Listvenites extend discontinuously 2–3 km long and 5–30 m wide in the southern part of the ophiolite, where light brown and orange-brown rocks form steep ridges along the SLZT (Liang et al. 2011). A Triassic flysch unit that weakly metamorphosed but intensely deformed is thrust over the ophiolitic massifs along the SLZT (Xu et al. 2015). The Triassic flysch unit consists of shale, siltstone, sandstone, and blocks of marble. Zhang et al. (2015) identified three alteration zones of listvenites, where the characteristics from south (thrust fault) to north (fresh harzburgite body) are silica-rich listvenites, talc-rich listvenites, and serpentine, respectively (Fig.1c). Their mineralogical analysis results of chromites further indicate that the parental rock of listvenites was shell-like dunite, which surrounded harzburgite. Most of the chromitite orebodies lie in the harzburgite near the contact with the transition zone dunite (Wang et al. 2010; Xiong et al. 2015). Individual chromitite bodies are lenticular, planar, podiform or irregular, mainly hosted in harzburgite, where they are commonly surrounded by dunite envelopes which are transitional to the peridotites (Wang et al. 1983; Zhou et al. 1996). The harzburgites are fresh, coarse-grained rocks with well-developed porphyroclastic textures, consisting mainly of forsterite (60–80 modal%) and orthopyroxene (10–30%) with minor clinopyroxene, magnesiochromite, and magnetite. The dunite envelopes are moderately fresh with massive textures, consisting mainly of 95 modal% forsterite, and < 5% magnesiochromite (Xu et al. 2009).

Previous mineralogical and geochemical studies indicate that the Luobusa mantle peridotites originally had a mid-ocean ridge basalt (MORB) affinity but that the podiform chromitites formed from hydrous boninitic magmas in a suprasubduction zone (SSZ)

125 environment (Zhou et al. 1996). Geochronological studies suggest that the two stages of
126 development, forming originally at a Tethyan spreading center at 177 ± 31 Ma (Zhou et al.
127 2002), followed by modification in the suprasubduction zone at ~126 Ma (Malpas et al.
128 2003). The SSZ ophiolites southward emplacement onto the proto-Indian continental
129 margin during the trench-continent collision around 110-90Ma (Xu et al. 2015). The only
130 known granitic rocks occurring in the northern part of the region belong to the Gangdese
131 batholith of the Lhasa block, which has a zircon U-Pb age of 91.5 ± 0.6 Ma (Zhang et al.
132 2015). The ophiolite was further displaced to this region during the India–Asia continental
133 collision and terminal closure of the Neotethyan basin from 55 to 35 Ma (Xu et al. 2015),
134 which clearly postdates the above plutonic activity around 90 Ma (Robinson et al. 2005).
135

136 ## OCCURRENCE AND PARAGENESIS

137 Tetrahedrite-(Ni) was found in silica-rich listvenites from the southern part of
138 Kangjinla district. The type material-hosted hand specimen is light blue to greyish green,
139 and almost all of the original minerals have disappeared except for the residual fragmented
140 magnesiochromite. Dolomite, magnesite, Cr-rich mica, Cr-bearing clinochlore, and quartz
141 are the most abundant secondary minerals as groundmass, with a small amount of
142 disseminated Ni-bearing aqueous arsenate (i.e., annabergite-hörnesite series, Ni-rich
143 hureaulite group minerals); Ni-bearing serpentine (i.e., antigorite-népouite series); Ni-rich
144 sulfosalts (i.e., gersdorffite, chalcostibite, vaesite, millerite, nickeline, tetrahedrite-(Ni),
145 tennantite-(Ni), Ni-rich tetrahedrite-(Fe), and Co-rich tetrahedrite-(Fe)) (Fig. 2).
146 The tetrahedrite-(Ni)-bearing listvenites have undergone at least two stages of
147 alteration. The first stage of alteration is serpentinization. At this stage, antigorite-népouite

148 series minerals and nickel-bearing sulfosalts were formed due to the alteration of olivine.
149 They were mostly obliterated during the superimposed transformation of late alterations,
150 metasomatic residues are only locally visible (Fig. 2b, d). The second stage is characterized
151 by the deposition of carbonate, Cr-rich mica, Cr-bearing clinochlore, and Ni-bearing
152 aqueous arsenate minerals. They occur in the two commonly observed mineral
153 assemblages: magnesite + dolomite ± quartz + Cr-rich mica + Cr-bearing clinochlore +
154 magnesiochromite + secondary chromite (Fig. 2a); and nickel-bearing sulfosalts + Ni-
155 bearing aqueous arsenate minerals ± magnesite ± quartz ± Cr-rich mica. They are
156 commonly formed along the edges of the first-stage mineral grains (Fig. 2b, c, d).

157 Tetrahedrite-(Ni) occurs as small composite inclusions in gersdorfite, consisting of
158 tetrahedrite-(Ni) + chalcostibite or tetrahedrite-(Ni) + vaesite. The anhedral-subhedral
159 granular crystals are commonly around 2–20 μm in size (Fig. 2e-h). Tetrahedrite-(Ni) is
160 black in colour and with a reddish black streak, the luster is metallic. Mohs hardness was
161 not measured, owing to the small size of the grain studied, but it should be 3–3½, close to
162 associated tetrahedrite-(Fe). It is brittle, with an indistinct cleavage and a conchoidal
163 fracture. Due to the small amount of available material and intergrowth of other phases,
164 density was not measured. The calculated density, based on the empirical formula and
165 single-crystal unit-cell parameters, is 5.073 g/cm^3. Tetrahedrite-(Ni) is opaque in
166 transmitted light and shows a steel grey colour in reflected light. Internal reflections were
167 not observed. Reflectance values measured in air using the SiC standard with Leica
168 microscope with a 20× objective and the four COM wavelengths (*R*) for tetrahedrite-(Ni)
169 are: 29.9 (470 nm), 29.2 (546 nm), 28.2 (589 nm) and 26.7 (650 nm). The full set of
170 reflectance values is given in Table 1, and the reflectivity curve is shown in Fig. 3.

This is the peer-reviewed, final accepted version for American Mineralogist, published by the Mineralogical Society of America.
The published version is subject to change. Cite as Authors (Year) Title. American Mineralogist, in press.
DOI: https://doi.org/10.2138/am-2022-8761. http://www.minsocam.org/

RAMAN SPECTROSCOPY

The Raman spectrum of tetrahedrite-(Ni) was collected at Tianjin Center, China Geological Survey, using a Renishaw in Via micro-Raman system with a laser with a frequency of 532 nm (power: 4 mW, spatial resolution: 1 μm), and equipped with a motorized x–y stage and a Leica microscope with a 50× objective. The back-scattered Raman signal was collected and the spectra were obtained from the polished thin section. The typical tetrahedrite-(Ni) Raman spectrum from 150 to 1500 cm^{-1} is shown in Fig. 4. In general, the major bands observed at 357 cm^{-1} can be attributed to vibrations of Sb-S bonds. The antisymmetric bending mode is medium band, which occurs at 297 cm^{-1} and 302 cm^{-1}. The weak band assigned to lattice vibrations occurs at 267 cm^{-1}.

CHEMICAL COMPOSITION

Quantitative chemical analyses were carried out at Central South University using a Shimadzu1720 electron probe microanalyzer. Analytical conditions were 15 kV accelerating voltage, 10 nA beam current, and a beam diameter of 1 μm. Standards (element, emission line) were: pure Cu (Cu*K*α), Ni (Ni*K*α), FeS_2 (Fe*K*α and S*K*α), Sb_2S_3 (Sb*L*α), and FeAsS (As*L*α). The ZAF correction was applied. Electron microprobe analysis data is given in Table 2.

The empirical formula calculated on the basis of 16 cations per formula unit, yielding the empirical formula $^{M(2)}Cu_6{}^{M(1)}[Cu_{4.03}(Ni_{1.55}Fe_{0.42})_{\Sigma 1.97}]_{\Sigma 6.00}{}^{X(3)}(Sb_{2.85}As_{1.16})_{\Sigma 4.01}S_{12.67}$, which can be simplified as $Cu_6[Cu_4(Ni,Fe)_2](Sb,As)_4S_{13}$. The ideal formula is $Cu_6(Cu_4Ni_2)Sb_4S_{13}$, which requires Cu 38.36, Ni 7.08, Sb 29.40, S 25.16, Total 100 wt.%.

X-RAY CRYSTALLOGRAPHY AND STRUCTURE DETERMINATION

The crystal for single XRD was extracted from the polished thin section by using an FEI Helios NanoLab 600i dual beam system equipped with Focused Ion beam (FIB) and scanning electron microscope (SEM). Single-crystal X-ray studies were carried out at Central South University, with a Rigaku XtaLAB Synergy diffractometer equipped with a Hybrid Pixel Array Detector and Cu$K\alpha$ radiation at 50 kV and 1 mA from a nearly equi-dimensional crystal (about 4 × 3 × 3 μm). The intensity data were corrected for X-ray absorption using the multi-scan method, and empirical absorption correction was performed using CrysAlisPro program spherical harmonics (Rigaku Oxford Diffraction, 2021), which was implemented in SCALE3 ABSPACK scaling algorithm. The refined unit-cell edge is a = 10.3478(4) Å and V = 1108.00(14) Å^3; the space group is $I\bar{4}3m$. The crystal structure was determined and refined using SHELX (Sheldrick 2015) and Olex2 software (Dolomanov et al. 2009).

The structure refinement revealed that the M(2)-site with triangular coordination, the tetrahedrally coordinated site S(1), and the octahedrally coordinated S(2)-site are fully occupied by Cu and S, respectively, while the tetrahedrally coordinated site M(1) is occupied by $Cu_{0.67}Ni_{0.24}Fe_{0.09}$, manually refined toward a minimum R_1 value and good agreement with the chemical data. The X(3) site with trigonal pyramidal coordination was refined to a joint occupancy of $Sb_{0.97}As_{0.03}$. After several cycles of anisotropic refinement for all the atoms, the R_1 converged to 0.0327 for 188 independent reflections with $F_o > 4\sigma$ (F_o) and 18 refined parameters. The details of the data collection and the final structure refinement are given in Table 3, the fractional atomic coordinates, occupation factors, and

displacement parameters in Table 4, anisotropic displacement parameters are listed in Table 5, selected bond distances in Table 6, and the bond-valence sums (BVS) obtained using the bond-valence parameters of Brese and O'Keeffe (1991) in Table 7 (CIF and table of structure factors and observations are available[1].)

Powder X-ray diffraction data were not measured due to the extremely small size of sample around 3 μm. Consequently, powder X-ray diffraction data, given in Table 8, were calculated using the software *VESTA* (Momma and Izumi 2011) on the basis of the structural model.

Results and Discussion

Crystal structure

Tetrahedrite-(Ni) is isostructural with other tetrahedrite group minerals with the general structural formula $^{M(2)}A_6{}^{M(1)}(B_4C_2)^{X(3)}D_4{}^{S(1)}Y_{12}{}^{S(2)}Z$ (Biagioni et al. 2020*a*). The tetrahedrally coordinated $M(1)S(1)_4$ forms a framework with large cavities. The $S(2)M(2)_6$ octahedrons are hosted in the cavities, and the cations at the *M*(2) site are coordinated as $M(2)S(1)_2S(2)$. The *X* (3) site is pyramidally coordinated $X(3)S(1)_3$, which forms the Laves polyhedron truncations (Foit Jr and Hughes 2004; Johnson et al. 1988; Moëlo et al. 2008). Because the ionic radius of $^{IV}Ni^{2+}$(0.53 Å) is smaller than that of $^{IV}Fe^{2+}$(0.66 Å) (Shannon 1981), a relatively short average bond distance (2.32 Å) of *M* (1)-S(1) for tetrahedrite-(Ni) has been observed, which decreased by 0.02 Å with the values for tetrahedrite-(Fe) determined by Johnson and Burnham (1985) (site occupied $Cu_{0.53}Fe_{0.24}$ with the bond length of M(1)-S(1) 2.34 Å). The calculated bond-valence sum (BVS) for *M*(1) site, given a 1.457 valence unit (vu), showed a little deviation from the theoretical value (1.333 vu),

240 which seems like a common phenomenon in the tetrahedrite group minerals (Biagioni et
241 al. 2020*b*, 2021, 2022; Mauro et al. 2021; Sejkora et al. 2021, 2022). As Biagioni et al.
242 (2020*b*) explained, for tetrahedrite-(Hg), due to the inaccuracy of the bond parameters for
243 the Hg-S pair or to a small shift of the S positions when the *M*(1) site is occupied by Hg.
244 The *M* (2) crystallographic position is occupied by monovalent cations that are bonded
245 to three S anions, forming a triangular "spinner blade" as described by Wuensch (1964). In
246 tetrahedrite-(Ni), *M* (2)-*S* (1) and *M* (2)-*S* (2) have an average bond distance of 2.265 Å
247 and 2.251 Å, respectively. The calculated BVS of *M* (2) site is 1.005 vu, which is perfectly
248 in agreement with the presence of monovalent cations. The *M*(2) sites at (1/2, Y, 1/2), as
249 shown in Table 5, anisotropic displacement parameters (ADP) U_{11}= U_{33}=0.084(3) Å are 4
250 times larger than that of U_{22}=0.019(3) Å, and U_{13} has a large negative value of -0.058(3)
251 Å. The abnormal ADP at *M* (2) site indicated that the Cu atoms vibrate with a large
252 amplitude along the -x+z direction perpendicular to the *M*(2)*S*(2)2*S*(1) triangular plane,
253 where x and z represent the crystal axes. We attempted to split the *M* (2) position, but it
254 did not significantly improve the structure refinement result, and the disorder was not
255 resolved in the refinement. This is a common feature, which is consistent with previous
256 studies on tetrahedrites (Biagioni et al. 2020*b*; Foit Jr and Hughes 2004; Welch et al. 2018).
257 The *X* (3) site has an average bond distance of 2.437 Å, and the value can be
258 comparable to the reported bond distance of the tetrahedrite series minerals (Biagioni et al.
259 2020*b*; Johnson and Burnham 1985; Rozhdestvenskaya et al. 1993). Some minor
260 differences due to the small amount of As^{3+} cations mixed occupancy at this site. The bond-
261 valence sum at *X* (3) site is 3.057 vu, which is consistent with the presence of $(Sb, As)^{3+}$.
262 The *S*(1) site is four-fold coordinated, being bonded to two *M*(1), one *M*(2), and one

263 *X*(3). *S*(2) is octahedrally coordinated by atoms hosted at *M*(2) sites. No vacancies were
264 observed at *S*(2) during the structure refinement. The BVS of the two S sites is 2.082 vu
265 and 2.008 vu, respectively.

266 **Formation temperature of tetrahedrite-(Ni)**

267 Tetrahedrite group minerals are extremely common in a variety of deposits worldwide.
268 Sack and Ebel (1993) concluded that the natural tetrahedrite-tennantite series minerals
269 crystallized over the 200–350 °C temperature range. The synthetic phase $Cu_{10.4}Ni_{1.6}Sb_4S_{13}$,
270 which is very close to the composition of our studied material, is stable up to 588 °C (e.g.,
271 at 607 °C it is no longer present, Barbier et al. 2015). Previous synthetic experiments
272 showed that the decomposition of the $Cu_{12}Sb_4S_{13}$ phase can lead to the formation of some
273 other phases at high temperature (Skinner et al. 1972; Pfitzner et al. 1997; Barbier et al.
274 2015). The mineral assemblages present for our tetrahedrite-(Ni)-bearing composite
275 inclusions (Figs. 2 e-g) indicate a complex Cu–Ni–Sb–As–S system. According to the
276 above synthetic observations, the paragenesis with chalcostibite ($CuSbS_2$) and the absence
277 of skinnerite (Cu_3SbS_3) suggest that tetrahedrite-(Ni) and its associated chalcostibite could
278 coexist stably at around 300–450 °C (Fig. 6). Although natural vaesite (NiS_2) from Katanga
279 yields a temperature of formation of 390 °C (Clark and Kullerud 1963), synthetic
280 experiments showed that vaesite might partially decompose into $Ni_{1-x}S$ and millerite (NiS)
281 phases at a temperature above 340 °C (Ferreira et al. 2019). In this study, we didn't find
282 millerite-bearing composite inclusions with tetrahedrite-(Ni). However, some euhedral
283 millerite and nickeline are often disseminated or have hydrous arsenate rings alone in
284 quartz and magnesite grains, so it seems to be formed later than tetrahedrite-(Ni), probably
285 during the listvenitization stage. Consequently, the mineral assemblages and synthesis

experiment results would suggest an approximate temperature of ~350 °C for the first tetrahedrite-(Ni) found in nature.

Geological significance

Nickel occurs extensively in the earth's crust, mantle, and core. As a siderophile, nickel prefers to form metals and thus was concentrated as Fe-Ni alloy in the core during the core-mantle differentiation process in the early history of the planet (McDonough and Sun 1995). While the concentration of nickel in the upper mantle and lower mantle can reach 0.15% and 0.20%, respectively, it is less than 100 ppm in the crust (Taylor and McLennan 1985; McDonough and Sun 1995; Barnes and Maier 1999). It is well known that Ni is a compatible element as long as Co and Cr, preferentially enter the crystalline mineral phase or residual phases under the conditions of phase equilibrium during partial melting or crystallization. Olivine has the largest nickel partition coefficient of any mantle silicate (Beattie et al. 1991), hosting almost 90% of all nickel in the mantle peridotites (Hoog et al. 2010). The ionic radius of $^{VI}Ni^{2+}$(0.69 Å) is similar to $^{VI}Mg^{2+}$(0.72 Å) (Shannon 1976), there can exist partial substitution between Ni and Mg atoms at the octahedral site in olivine. The Ni concentration in olivine derived from typical mantle peridotites is about 0.2%-0.3% (Herzberg et al. 2013).

Tetrahedrite-(Ni) was found in listvenite, and its parental rock was considered to be dunite envelopes (Zhang et al. 2015). The fresh dunite envelopes from Luobusa mantle peridotites, consist mainly of 95 modal% olivine (forsterite), and < 5% magnesiochromite. Previous whole-rock chemical analyses revealed that hosting peridotite contains 0.33 % NiO and forsterite has an average Ni concentration of 0.40% (Xu et al. 2009). Therefore, it is not surprising that 95 modal % of the forsterite in the original dunite were completely

309 altered and the Ni released from the octahedral site subsequently formed quite a few Ni-
310 bearing serpentine and Ni-rich sulfosalts.

311 As described by Boskabadi et al. (2020), transformation of mantle peridotites to
312 listvenites usually starts with lizardite serpentinization, and is followed by
313 contemporaneous carbonation and antigorite serpentinization, antigorite-talc-magnesite
314 alteration, finally producing typical listvenite with the characteristical minerals [Cr-bearing
315 muscovite (illite) ± Cr-bearing chlorite, Halls and Zhou 1995]. Serpentinites originate from
316 the hydration of olivine-dominated ultramafic rocks (with H_2O content up to 15–16 wt.%)
317 (Evans et al. 2013; Guilot and Hattori 2013), and oxygen isotope fractionation suggests
318 that serpentinization starts at a high temperature, in the range of 300–500 °C (Mével 2003).
319 It has been known for some time that all serpentinites play essential roles not only in
320 incorporating water but also in substantially enriching fluid-mobile elements (such as Sb
321 and As), regardless of their origin (MORB or SSZ) or eventual geological location
322 (Deschamps et al. 2012, 2013; Guilot and Hattori 2013). Since ultrabasic rocks themselves
323 have few of these fluid-mobile elements, the Sb/As-bearing fluids resulting from the
324 dehydration of metasediments could be a good candidate for the source of the Sb/As
325 enrichments in the Luobusa serpentinites.

326 Ferenc et al. (2016) found gersdorffite and millerite in the listvenite from Muránska
327 Zdychava, which is similar to what we found in Luobusa listvenite, and they suggested
328 these sulfosalts form during the serpentinization stage and precipitation of Ni and Co
329 sulphoarsenides is typical of advanced serpentinization to listvenitization. Previous studies
330 show that, differently from the mineral assemblage of low-temperature listvenites, in the
331 higher-temperature related listvenites, different lithological zones composed of distinctive

332 mineral assemblages (serpentine ± magnesite, magnesite + talc, and magnesite + quartz)
333 commonly record the stepwise carbonation reactions of serpentinites (Menzel et al. 2018).
334 The presence of the unusual Cr-rich chlorite and Cr-bearing mica (illite) in particular
335 indicates the conditions under which listvenite are formed correspond to temperatures
336 ranging from 270 to 340 °C and pressures ranging from 0.10 to 0.30 GPa (Halls and Zhou
337 1995; Spiridonov 1991). These mineral assemblages and temperature range are very
338 consistent with our case (Fig. 2) and similar to the P–T conditions (350 °C, 0.20 GPa) of
339 Muránska Zdychava listvenite assumed by Ferenc et al. (2016). For the further alteration,
340 the SLZT structure from the southern part of Kangjinla district plays a key role during the
341 process of listvenitization as it could be the channel of the CO_2-rich fluids that transform
342 the serpentinite into the carbonate–quartz listvenite. The aqueous arsenates around the
343 gersdorffite in the Luobusa listvenite, possibly formed by the metasomatism of primary
344 Ni-containing sulfosalts by atmospheric water entering along the deep SLZT fault in the
345 shallow crust lever under a low temperature condition after the listvenite emplacement.
346 Consequently, previous geochemical studies and this study of mineralogical
347 characteristics suggest that the listvenite body from the Luobusa chromitite deposit formed
348 in three principal evolution stages:
349 (1) peridotite stage: nickel, as a compatible element, enters the octahedral site of forsterite
350 through partial substitution from the deep earth;
351 (2) serpentinization stage: this stage may occur in the SSZ environment, with strong
352 serpentinization, Ni^{2+} cations released by the dissolution of forsterite react with the Sb/As
353 containing fluid to form tetrahedrite-(Ni) and associated sulfosalts;
354 (3) listvenitization stage: the most likely environment for listvenitization is a prograde

355 metamorphic event post-dating serpentinization, possibly related to further displacement
356 of the Luobusa ophiolites caused by the closure of the Neotethyan basin and the hard
357 collision of Greater India with Asia.
358
359 **Implications**
360 Tetrahedrite-(Ni), as the first natural nickel end-member mineral of the tetrahedrite
361 group, formed in the post-serpentinization associated stage at a moderately high
362 temperature of around 350 °C. According to its special formation process and its mineral
363 assemblage, tetrahedrite-(Ni) could be considered as a potential geothermometer of
364 ultrabasic rock serpentinization environments.
365 The temperature of formation of tetrahedrite-(Ni) appears to be slightly higher than
366 other tetrahedrites (< 350 °C) in epithermal deposits, which may be the main reason why
367 tetrahedrite-(Ni) is rarely found in nature. According to the geochemical properties of
368 nickel, post-serpentinized peridotite may be a potential rock to host other nickel-
369 endmember series of tetrahedrite minerals.
370 The nickel-rich tetrahedrite phases with low production cost, large *ZT* and
371 environmentally friendly components, have been considered as a good candidate for large-
372 scale TE material applications (Barbier et al.2015; Lu et al. 2015; Suekuni et al. 2013),
373 while the naturally occurring tetrahedrite-(Ni) may serve as an important reference in this
374 field.
375
376 **Acknowledgements**
377 Jiří Sejkora, an anonymous reviewer, associate editor Oliver Tschauner, and editor

Hongwu Xu are thanked for their constructive comments on the manuscript. This study was supported by the Natural Science Foundation of China (42072054), National Key R&D Programmes (92062105) and China Scholarship Council (CSC) 202106400047, 202108575009).

References cited

Barbier, T., Lemoine, P., Gascoin, S., Lebedev, O. I., Kaltzoglou, A., Vaqueiro, P., Powell, A.V., Smith, R.I., and Guilmeau, E. (2015) Structural stability of the synthetic thermoelectric ternary and nickel-substituted tetrahedrite phases. Journal of Alloys and Compounds, 634, 253–262.

Barnes, S.J., and Maier, W.D. (1999) The fractionation of Ni, Cu and the noble metals in silicate and sulphide liquids. Geological Society Canada Mineralogical Society Canada, short course notes, 13, 69–106.

Beattie, P., Ford, C., and Russell, D. (1991) Partition coefficients for olivine-melt and orthopyroxene-melt systems. Contributions to Mineralogy and Petrology, 109, 212–224.

Biagioni, C., George, L.L., Cook, N.J., Makovicky, E., Moëlo, Y., Pasero, M., Sejkora, J., Stanley, C.J., Welch, M.D., and Bosi, F. (2020a) The tetrahedrite group: Nomenclature and classification. American Mineralogist, 105, 109–122.

Biagioni, C., Sejkora, J., Musetti, S., Velebil, D., and Pasero, M. (2020b). Tetrahedrite-(Hg), a new ‘old’member of the tetrahedrite group. Mineralogical Magazine, 84, 584–592.

Biagioni, C., Sejkora, J., Raber, T., Roth, P., Moëlo, Y., Dolníček, Z., and Pasero, M. (2021) Tennantite-(Hg), $Cu_6(Cu_4Hg_2)As_4S_{13}$, a new tetrahedrite-group mineral from the

Lengenbach quarry, Binn, Switzerland. Mineralogical Magazine, 85, 744–751.

Biagioni, C., Kasatkin, A., Sejkora, J., Nestola, F., and Škoda, R. (2022) Tennantite-(Cd), $Cu_6(Cu_4Cd_2)As_4S_{13}$, from the Berenguela mining district, Bolivia: the first Cd-member of the tetrahedrite group. Mineralogical Magazine, DOI: 10.1180/mgm.2022.61.

Boskabadi, A., Pitcairn, I. K., Leybourne, M.I., Teagle, D. A., Cooper, M.J., Hadizadeh, H., Bezenjani, R.N., and Bagherzadeh, R.M. (2020) Carbonation of ophiolitic ultramafic rocks: Listvenite formation in the Late Cretaceous ophiolites of eastern Iran. Lithos, 352–353, 105307.

Brese, N.E., and O'Keeffe, M. (1991) Bond-valence parameters for solids. Acta Crystallographica, B47, 192–197.

Brown, I.D. (1977) Predicting bond lengths in inorganic crystals. Acta Crystallographica Section B: Structural Crystallography and Crystal Chemistry, 33, 1305–1310.

Carrozzini, B., Garavelli, C.L., and Vurro, F. (1991) Tetrahedrite (supposed "Frigidite") and associated Ni minerals from Frigido mine (Apuane Alps). Periodico di Mineralogia, 60, 5–14.

Charlat, M., and Lévy, C. (1976) Influence des principales substitutions sur les propriétés optiques dans la série tennantite-tétraédrite. Bulletin de la Société française de Minéralogie et de Cristallographie, 99, 29–37.

Clark, L.A., and Kullerud, G. (1963) The sulfur-rich portion of the Fe-Ni-S system. Economic Geology, 58, 853–885.

D'Achiardi, A. (1881) Su di alcuni minerali della miniera del Frigido presso Massa nelle Alpi Apuane. Atti della Società Toscana di Scienze Naturali, Processi Verbali, 2,

171–178.

Deschamps, F., Godard, M., Guillot, S., Chauvel, C., Andreani, M., Hattori, K., Wuder, B., and France, L. (2012) Behavior of fluid-mobile elements in serpentines from abyssal to subduction environments: Examples from Cuba and Dominican Republic. Chemical Geology, 312, 93–117.

Deschamps, F., Godard, G., Guillot S., and Hattori, K. (2013) Geochemistry of subduction zone serpentinites: a review. Lithos, 178, 96–127.

Dolomanov, O.V., Bourhis, L.J., Gildea, R.J., Howard, J.A.K., and Puschmann, H. (2009) A complete structure solution, refinement and analysis program. Journal of Applied Crystallography, 42, 339–341.

Evans, B.W., Hattori, K., and Baronnet, A. (2013) Serpentinite: what, why, where?. Elements, 9, 99–106.

Ferenc, S., Uher, P., Spišiak, J., and Šimonová, V. (2016) Chromium-and nickel-rich micas and associated minerals in listvenite from the Muránska Zdychava, Slovakia: products of hydrothermal metasomatic transformation of ultrabasic rock. Journal of Geosciences, 61, 239–254.

Ferreira, H.M., Lopes, E.B., Malta, J.F., Ferreira, L.M., Casimiro, M.H., Santos, L., Pereira, M.F.C., and Gonçalves, A.P. (2019) Preparation, thermal stability and electrical transport properties of vaesite, NiS_2, PeerJ Materials Science, 1, e2.

Foit Jr, F.F., and Hughes, J.M. (2004) Structural variations in mercurian tetrahedrite. American Mineralogist, 89, 159–163.

Guillot, S., and Hattori, K. (2013) Serpentinites: essential roles in geodynamics, arc volcanism, sustainable development, and the origin of life. Elements, 9, 95–98.

447 Herzberg, C., Asimow, P.D., Ionov, D.A., Vidito, C., Jackson, M.G., and Geist, D. (2013)
448 Nickel and helium evidence for melt above the core-mantle boundary. Nature, 493,
449 393–397.
450 Halls, C., and Zhao, R. (1995) Listvenite and related rocks: perspectives on terminology
451 and mineralogy with reference to an occurrence at Cregganbaun, Co. Mayo,
452 Republic of Ireland. Mineralium Deposita, 30, 303–313.
453 Hoog, J.C.M.D., Gall, L., and Cornell, D.H. (2010) Trace-element geochemistry of mantle
454 olivine and application to mantle petrogenesis and geothermobarometry. Chemical
455 Geology, 270, 196–215.
456 Johnson, M.L., and Burnham, C.W. (1985) Crystal structure refinement of an arsenic-
457 bearing argentian tetrahedrite. American Mineralogist, 70, 165–170.
458 Johnson, N.E., Craig, J.R., and Rimstidt, J.D. (1988) Crystal chemistry of tetrahedrite.
459 American Mineralogist, 73, 389–397.
460 Liang, F.H., Xu, Z.Q., Ba, D.Z., Xu, X.Z., Liu, F., Xiong, F.H., and Jia, Y. (2011) Tectonic
461 occurrence and emplacement mechanism of ophiolite from Luobusha–Zedang,
462 Tibet. Acta Petrologica Sinica 27, 3255–3268 (in Chinese with English abstract).
463 Lu, X., Morelli, D.T., Xia, Y., and Ozolins, V. (2015) Increasing the Thermoelectric Figure
464 of Merit of Tetrahedrites by Co-Doping with Nickel and Zinc. ChemInform, 46,
465 408–413.
466 Makovicky, E., and Karup-Møller, S. (1994) Exploratory studies on substitution of minor
467 elements in synthetic tetrahedrite. Part I. Substitution by Fe, Zn, Co, Ni, Mn, Cr, V
468 and Pb. Unit-cell parameter changes on substitution and the structural role of "Cu^{2+}".
469 Neues Jahrbuch für Mineralogie Abhandlungen, 167, 89–123.

Malpas, J., Zhou, M.F., Robinson, P.T., and Reynolds, P. (2003) Geochemical and geochronological constraints on the origin and emplacement of the Yarlung-Zangbo ophiolites, Southern Tibet. In: Dilek, Y., Robinson, P.T. (ed.), Ophiolites Through Earth History. Geological Society, London, Special Publications, 218, 191–206.

Mauro, D., Biagioni, C., and Zaccarini, F. (2021) New data on gersdorffite and associated minerals from the Peloritani Mountains (Sicily, Italy). European Journal of Mineralogy, 33, 717–726.

McDonough, W.F., and Sun, S.S. (1995) The composition of the Earth. Chemical Geology, 120, 223–253.

Menzel, M.D., Garrido, C.J., Sánchez-Vizcaíno, V.L., Marchesi, C., Hidas, K., Escayola, M.P., and Huertas, A.D. (2018) Carbonation of mantle peridotite by CO_2-rich fluids: the formation of listvenites in the Advocate ophiolite complex (Newfoundland, Canada). Lithos, 323, 238–261.

Mével, C. (2003) Serpentinization of abyssal peridotites at mid-ocean ridges. Comptes Rendus Geoscience, 335, 825–852.

Moëlo, Y., Makovicky, E., Mozgova, N. N., Jambor, J. L., Cook, N., Pring, A., Paar, W., Nickel, E.H., Graeser, S., Karup-Møller, Žunic, T.B., Mumme, W.G., Vurro, F., Topa, D., Bindi, L., Bente, K., and Shimizu, M. (2008) Sulfosalt systematics: a review. Report of the sulfosalt sub-committee of the IMA Commission on Ore Mineralogy. European Journal of Mineralogy, 20, 7–46.

Momma, K., and Izumi, F. (2011) VESTA 3 for three-dimensional visualization of crystal, volumetric and morphology data. Journal of Applied Crystallography, 44, 1272–

1276.

Nicolas, A., Girardeau, J., Marcoux, J., Duprè, B., Wang, X.B., Cao, Y.G., Zeng, H.X., and Xiao, X.C. (1981) The Xigaze ophiolite (Tibet): A peculiar oceanic lithosphere. Nature, 294, 414–417.

Pfitzner, A., Evain, M., and Petricek, V. (1997) $Cu_{12}Sb_4S_{13}$: A temperature-dependent structure investigation. Acta Crystallographica Section B: Structural Science, 53, 337–345.

Phillips, R. (1819) Analysis of the copper ore, described in the preceding paper. The Quarterly Journal of Science, Literature and the Arts, 7, 100–102.

Phillips, W. (1819) Description of an ore of copper from Cornwall. The Quarterly Journal of Science, Literature and the Arts, 7, 95–100.

Rigaku Oxford Diffraction. (2021) CrysAlisPro Software system, version 1.171.41.96a. Rigaku Corporation.

Robinson, P.T., Malpas, J., Zhou, M.F., Ash, C., Yang, J.S., and Bai, W.J. (2005) Geochemistry and Origin of Listwanites in the Sartohay and Luobusa Ophiolites, China. International Geology Review, 47, 177–202.

Rozhdestvenskaya, I.V., Zayakina, N.V., and Samusikov, V.P. (1993) Crystal structure features of minerals from a series of tetrahedrite-freibergite. Mineralogiceskij Zhurnal, 15, 9–17.

Sack, R.O., and Ebel, D.S. (1993). As-Sb exchange energies in tetrahedrite-tennantite fahlores and bournonite-seligmannite solid solutions. Mineralogical Magazine, 57, 635–642.

Sejkora, J., Biagioni, C., Vrtiška, L., and Moëlo, Y. (2021) Zvěstovite-(Zn), $Ag_6(Ag_4Zn_2)$

516 As_4S_{13}, a new tetrahedrite-group mineral from Zvěstov, Czech Republic.
517 Mineralogical Magazine, 85, 716–724.
518 Sejkora, J., Biagioni, C., Števko, M., Raber, T., Roth, P., and Vrtiška, L. (2022)
519 Argentotetrahedrite-(Zn), $Ag_6(Cu_4Zn_2)Sb_4S_{13}$, a new member of the tetrahedrite
520 group. Mineralogical Magazine, 86, 319–330.
521 Serranti, S., Ferrini, V., Masi, U., and Cabri, L.J. (2002) Trace-element distribution in
522 cassiterite and sulfides from rubané and massive ores of the Corvo deposit, Portugal.
523 The Canadian Mineralogist, 40, 815–835.
524 Shannon, R.D. (1976) Revised effective ionic radii and systematic studies of interatomic
525 distances in halides and chalcogenides. Acta crystallographica section A: crystal
526 physics, diffraction, theoretical and general crystallography, 32, 751–767.
527 Shannon, R.D. (1981) Bond distances in sulfides and a preliminary table of sulfide crystal
528 radii. Structure and Bonding in Crystals, 2, 53–70.
529 Sheldrick, G.M. (2015) SHELXT–Integrated space-group and crystal structure
530 determination. Acta Crystallographica, A71, 3–8.
531 Skinner, B.J., Luce, F.D., and Makovicky, E. (1972) Studies of the sulfosalts of copper III;
532 Phases and phase relations in the system Cu-Sb-S. Economic Geology, 67, 924–
533 938.
534 Spiridonov, E.M. (1991) Listvenites and zodites. International geology review, 33, 397–
535 407.
536 Suekuni, K., Tsuruta, K., Kunii, M., Nishiate, H., Nishibori, E., Maki, S., Ohta, M.,
537 Yamamoto, A., and Koyano M. (2013) High-performance thermoelectric mineral
538 $Cu_{12-x}Ni_xSb_4S_{13}$ tetrahedrite. Journal of Applied Physics, 113, 536.

539 Taylor, S.R., and McLennan, S.M. (1985) The continental crust: its composition and
540 evolution. Blackwell, London, 312 pp.
541 Wang, H.S., Bai, W.J., Wang, B.X., and Chai, Y.C. (1983) Chromite Deposits in China
542 and Their Origin. Science Press, Beijing, 227 pp. (in Chinese).
543 Wang, X.B., Zhou, X., and Hao, Z.G. (2010) Some opinions on further exploration for
544 chromite deposits in the Luobusa area, Tibet, China. Geological Bulletin of China,
545 29, 105–114 (in Chinese with English abstract).
546 Wang, Y.J., Chen, R.J., Gu, X.P., Hou, Z.Q., Yang, Z.Q., Dong, G.C., Guo, H., and Qu, K.
547 (2021) Tetrahedrite-(Ni), IMA2021-031. CNMNC Newsletter 62. Mineralogical
548 Magazine, 85, 637.
549 Warr, L.N. (2021) IMA–CNMNC approved mineral symbols. Mineralogical Magazine, 85,
550 291–320.
551 Welch, M.D., Stanley, C.J., Spratt, J., and Mills, S.J. (2018) Rozhdestvenskayaite
552 $Ag_{10}Zn_2Sb_4S_{13}$ and argentotetrahedrite $Ag_6Cu_4(Fe^{2+},Zn)_2Sb_4S_{13}$: two Ag-dominant
553 members of the tetrahedrite group. European Journal of Mineralogy, 30, 1163–1172.
554 Wuensch, B. J. (1964) The crystal structure of tetrahedrite, Cu12Sb4S18. Zeitschrift für
555 Kristallographie-Crystalline Materials, 119, 437–453.
556 Xiong, F.H., Yang, J.S., Ba, D.Z., Liu, Z., Xu, X.Z., Feng, G.Y., Niu, X.L., and Xu J.F.
557 (2014) Different type of chromitite and genetic model from Luobusa ophiolite,
558 Tibet. Acta Petrologica Sinica, 30, 2137–2163 (in Chinese with English Abstracts).
559 Xiong, F.H., Yang, J.S., Robinson, P. T., Xu, X.Z., Liu, Z., Li, Y., Li, J.Y, and Chen, S.Y.
560 (2015) Origin of podiform chromitite, a new model based on the Luobusa ophiolite,
561 Tibet. Gondwana Research, 27, 525–542.

562 Xu, X.Z. (2009) Origin of the Kangjinla podiform chromite deposit and mantle peridotite,
563 South Tibet. Ph.D. Dissertation. Beijing: Chinese Academy of Geological Sciences,
564 1–165 (in Chinese with English Abstracts).
565 Xu, Z.Q., Dilek, Y., Yang, J.S., Liang, H.F., Liu, F., Ba, D.Z., Cai, Z.H., Li, G.W., Dong,
566 H.W., and Ji, S.C. (2015) Crustal structure of the Indus–Tsangpo suture and its
567 ophiolites in southern Tibet. Gondwana Research, 27, 507–524.
568 Yang, J.S., Bai, W.J., Fang, Q.S., Yan, B.G., Rong, He., and Chen, S.Y. (2004) Coesite
569 discovered from the podiform chromitite in the Luobusa ophiolite, Tibet. Earth
570 Science: Journal of China University of Geosciences, 29, 651–660 (in Chinese with
571 English abstract).
572 Zhang, L., Yang, J.S., Robinson, P.T., Xiong, F.H., Chen, Y.H., Lai, S.M., and Chen, M.
573 (2015) Origin of listwanite in the Luobusa ophiolite, Tibet, implications for
574 chromite stability in hydrothermal systems. Acta Geologica Sinica-English Edition,
575 89, 402–417.
576 Zhou, M.F., Robinson, P.T., Malpas, J., and Li, Z. (1996) Podiform chromitites from the
577 Luobusa ophiolite (southern Tibet): implications for melt–rock interaction and
578 chromite segregation. Journal of Petrology, 37, 3–21.
579 Zhou, S., Mo, X.X., Mahony, J.J., Zhang, S.Q., Guo, T.Y., and Zhao, Z.D. (2002)
580 Geochronology and Nd and Pb isotope characteristics of gabbro dikes in the
581 Luobusha ophiolite, Tibet. Chinese Science Bulletin, 47, 143–146 (in Chinese with
582 English abstract).
583

584 # Table Captions

585 **TABLE 1** – Reflectance data for tetrahedrite-(Ni) from Luobusa chromite deposit

586 **TABLE 2** – Chemical data (wt. %) for tetrahedrite-(Ni)

587 **TABLE 3** – Information on structural refinement for tetrahedrite-(Ni)

588 **TABLE 4** – Site, Wyckoff position, site occupancy factors (s.o.f.), fractional atomic
589 coordinates and equivalent isotropic displacement parameters (in $Å^2$) for tetrahedrite-(Ni)

590 **TABLE 5 –** Anisotropic displacement parameters (in $Å^2$) for tetrahedrite-(Ni)

591 **TABLE 6 –** Selected bond distances (Å) for tetrahedrite-(Ni)

592 **TABLE 7 –** Bond-valence (*vu*) calculation for tetrahedrite-(Ni)

593 **TABLE 8 –** Caluculated X-ray powder diffraction data (*d* in Å) for tetrahedrite-(Ni)
594

595 # Figure Captions

596 **FIGURE 1** – Simplified geological map of the Luobusa ophiolite, Tibet (modified after
597 Xiong et al. 2014; Zhang et al. 2015)

598 1. Granite; 2. Tertiary Luobusa Formation; 3. Upper Triassic Flysch; 4. Upper Cretaceous
599 Zedang Formation; 5. Cumulate rock; 6. Dunite; 7. Harzburgite; 8. Serpentinite Zone III;
600 9. Listvenite Zone II; 10. Listvenite Zone I; 11. Podiform chromitite; 12. Unconformity;
601 13. Fault; 14. Thrust contact; 15. Sampling location

602 **FIGURE 2** – Back scattered electron (a-d) and plane-polarized reflected light images (e-h)
603 of the occurrence and mineral association of tetrahedrite-(Ni). Mineral symbols are quoted
604 from Warr (2021).
605 (**a**) Fragmented residual magnesiochromite (Mchr) with secondary Cr-rich mica (Cr-Mc),
606 Cr-rich clinochlore (Cr-Clc) and magnesite (Mgs)
607 (**b**) Residual gersdorffite (Gdf) and népouite (Npo) with secondary annabergite (Anb) and
608 *Ni-dominant irhtemite* in magnesite, dolomite (Dol), and quartz (Qz) matrix

(**c**) Annabergite formed along the edges of the primary gersdorffite (top left), partially metasomatic alteration of gersdorffite by annabergite (down right)

(**d**) Gersdorffite was almost completely replaced by annabergite, dolomite and quartz, a small amount of népouite residues is on the edge, but the euhedral crystal morphology of the original gersdorffite is still clear

(**e**) Tetrahedrite-(Ni) (Ttr-Ni) and chalcostibite (Ccsb) inclusions within gersdorffite in dolomite matrix

(**f-h**) Tetrahedrite-(Ni) and vaesite (Va) inclusions within gersdorffite in dolomite matrix

FIGURE 3 – Reflectance curves of tetrahedrite-(Ni) in air. For comparison, the reflectance curves of other members of the tetrahedrite series are shown: tetrahedrite-(Hg), Buca della Vena (Biagioni et al. 2020b); tetrahedrite-(Fe), T18 and tetrahedrite-(Zn), M12 (Charlat and Lévy 1976).

FIGURE 4 – Raman spectrum of tetrahedrite-(Ni)

FIGURE 5 – Crystal structure of tetrahedrite-(Ni) plotted using Olex2 (Dolomanov et al. 2009)

FIGURE 6 – Temperature dependence of the weight fraction of each phase in the Cu-Sb-S system, modified after Barbier et al. (2015)

Table Captions

TABLE 1 – Reflectance data for tetrahedrite-(Ni) from Luobusa chromite deposit

TABLE 2 – Chemical data (wt. %) for tetrahedrite-(Ni)

TABLE 3 – Information on structural refinement for tetrahedrite-(Ni)

TABLE 4 – Site, Wyckoff position, site occupancy factors (s.o.f.), fractional atomic coordinates and equivalent isotropic displacement parameters (in $Å^2$) for tetrahedrite-(Ni)

TABLE 5 – Anisotropic displacement parameters (in $Å^2$) for tetrahedrite-(Ni)

TABLE 6 – Selected bond distances (Å) for tetrahedrite-(Ni)

TABLE 7 – Bond-valence (*vu*) calculation for tetrahedrite-(Ni)

TABLE 8 – Caluculated X-ray powder diffraction data (*d* in Å) for tetrahedrite-(Ni)

Figure Captions

FIGURE 1 – Simplified geological map of the Luobusa ophiolite, Tibet (modified after Xiong et al. 2014; Zhang et al. 2015)

1. Granite; 2. Tertiary Luobusa Formation; 3. Upper Triassic Flysch; 4. Upper Cretaceous Zedang Formation; 5. Cumulate rock; 6. Dunite; 7. Harzburgite; 8. Serpentinite Zone III; 9. Listvenite Zone II; 10. Listvenite Zone I; 11. Podiform chromitite; 12. Unconformity; 13. Fault; 14. Thrust contact; 15. Sampling location

FIGURE 2 – Back scattered electron (a-d) and plane-polarized reflected light images (e-h) of the occurrence and mineral association of tetrahedrite-(Ni). Mineral symbols are quoted from Warr (2021).

(**a**) Fragmented residual magnesiochromite (Mchr) with secondary Cr-rich mica (Cr-Mc), Cr-rich clinochlore (Cr-Clc) and magnesite (Mgs)

(**b**) Residual gersdorffite (Gdf) and népouite (Npo) with secondary annabergite (Anb) and *Ni-dominant irhtemite* in magnesite, dolomite (Dol), and quartz (Qz) matrix

(**c**) Annabergite formed along the edges of the primary gersdorffite (top left), partially metasomatic alteration of gersdorffite by annabergite (down right)

(**d**) Gersdorffite was almost completely replaced by annabergite, dolomite and quartz, a small amount of népouite residues is on the edge, but the euhedral crystal morphology of the original gersdorffite is still clear

(**e**) Tetrahedrite-(Ni) (Ttr-Ni) and chalcostibite (Ccsb) inclusions within gersdorffite in dolomite matrix

(**f-h**) Tetrahedrite-(Ni) and vaesite (Va) inclusions within gersdorffite in dolomite matrix

FIGURE 3 – Reflectance curves of tetrahedrite-(Ni) in air. For comparison, the reflectance curves of other members of the tetrahedrite series are shown: tetrahedrite-(Hg), Buca della Vena (Biagioni et al. 2020b); tetrahedrite-(Fe), T18 and tetrahedrite-(Zn), M12 (Charlat and Lévy 1976).

FIGURE 4 – Raman spectrum of tetrahedrite-(Ni)

FIGURE 5 – Crystal structure of tetrahedrite-(Ni) plotted using Olex2 (Dolomanov et al. 2009)

FIGURE 6 – Temperature dependence of the weight fraction of each phase in the Cu-Sb-S system, modified after Barbier et al. (2015)

This is the peer-reviewed, final accepted version for American Mineralogist, published by the Mineralogical Society of America.
The published version is subject to change. Cite as Authors (Year) Title. American Mineralogist, in press.
DOI: https://doi.org/10.2138/am-2022-8761. http://www.minsocam.org/

TABLE 1. Reflectance data for tetrahedrite-(Ni) from Luobusa chromite deposit

R	λ (nm)	R	λ (nm)
28.2	400	28.9	560
29.0	420	28.4	580
29.5	440	28.2	589 (COM)
29.8	460	27.9	600
29.9	470 (COM)	27.4	620
29.9	480	26.9	640
29.9	500	26.7	650 (COM)
29.6	520	26.5	660
29.3	540	26.1	680
29.2	546 (COM)	25.9	700

TABLE 2. Chemical data (wt. %) for tetrahedrite-(Ni)

Element	Mean	Range	Stand. Dev. (σ)	*apfu*
Cu	39.83	37.38-42.52	2.02	10.03
Ni	5.67	4.10-7.90	1.65	1.55
Fe	1.45	0.40-2.36	0.72	0.42
Sb	21.69	19.09-24.44	2.3	2.85
As	5.45	3.36-6.57	1.13	1.16
S	25.39	24.10-26.61	0.69	12.67
Total	99.48			

TABLE 3. Information on structural refinement for tetrahedrite-(Ni)

Crystal data	
Structural formula	$Cu_{10.02}Ni_{1.44}Fe_{0.54}Sb_{3.85}As_{0.15}S_{13}$
Formula weight	1647.66
Crystal size/μm	4×3×3
Crystal system	cubic
Space group	$I\bar{4}3m$ (#217)
Unit cell dimensions	a = 10.3478(4) Å
Volume	1108.00(14) $Å^3$
Z	2
Data collection and refinement	
Instrument	Rigaku Synergy
Radiation, wavelength, temperature	Cu $K\alpha$, 1.54184 Å, 293(2) K
$F(000)$	1508
2θ range (°)	12.096 to 130.01
Total reflections	1881
Unique ref (all)	200
Unique ref [$I > 4\sigma(I)$]	188
R_{int}	0.1116
R_σ	0.0563
Range of h, k, l	$-6 \le h \le 12$; $-12 \le k \le 12$; $-12 \le l \le 11$
R_1, wR_2 [$I > 4\sigma(I)$]	R_1 = 0.0327, wR_2 = 0.0598
R_1, wR_2 [all data]	R_1 = 0.0389, wR_2 = 0.0614
Goodness-of-fit	1.182
No. of parameters, restraints	18, 0
Maximum and minimum residual peak (e $Å^{-3}$)	0.62 [1.47Å from X(3)] -0.73[0.41 Å from S(2)]

This is the peer-reviewed, final accepted version for American Mineralogist, published by the Mineralogical Society of America.
The published version is subject to change. Cite as Authors (Year) Title. American Mineralogist, in press.
DOI: https://doi.org/10.2138/am-2022-8761. http://www.minsocam.org/

TABLE 4. Site, Wyckoff position, site occupancy factors (s.o.f.), fractional atomic coordinates and equivalent isotropic displacement parameters (in Å^2) for tetrahedrite-(Ni)

Site	*Wyck.*	*s.o.f*	*x/a*	*y/b*	*z/c*	U_{eq}
M(2)	12*e*	$Cu_{1.00}$	0	0.2176(7)	0	0.062 (2)
M(1)	12*d*	$Cu_{0.67}Ni_{0.24}Fe_{0.09}$	3/4	1/2	0	0.0204(15)
X(3)	8*c*	$Sb_{0.96(4)}As_{0.04(4)}$	0.73152(11)	0.26848(11)	0.73152(11)	0.0166(7)
S(1)	24*g*	$S_{1.00}$	0.8842(3)	0.3627(4)	0.8842(3)	0.0166(12)
S(2)	2*a*	$S_{1.00}$	0	0	0	0.018(3)

TABLE 5. Anisotropic displacement parameters (in Å^2) for tetrahedrite-(Ni)

Site	U_{11}	U_{22}	U_{33}	U_{23}	U_{13}	U_{12}
M(2)	0.084(3)	0.019(3)	U_{11}	0	-0.058(3)	0
M(1)	0.026(3)	0.0175(17)	U_{22}	0	0	0
X(3)	0.0166(7)	U_{11}	U_{11}	0.0026(5)	-0.0026(5)	U_{23}
S(1)	0.0167(15)	0.016(3)	U_{11}	-0.0012(12)	-0.0018(17)	-0.0012(12)
S(2)	0.018(3)	U_{11}	U_{11}	0	0	0

TABLE 6. Selected bond distances (Å) for tetrahedrite-(Ni)

Cu2—S1$^{\times 2}$	2.265(5)	Cu1—S1$^{\times 4}$	2.320(3)
—S2$^{\times 1}$	2.251(7)		
Mean	2.260	Sb—S1$^{\times 3}$	2.437(5)

TABLE 7. Bond-valence (*vu*) calculation for tetrahedrite-(Ni)

Site	*M*(2) (Cu)	*M*(1) ($Cu_{0.67}Ni_{0.24}Fe_{0.09}$)	*X*(3) ($Sb_{0.96}As_{0.04}$)	Sum.	Theor.
S(1)	0.335$^{\times 2\downarrow}$	0.364$^{\times 4\downarrow \times 2\rightarrow}$	1.019$^{\times 3\downarrow}$	2.082	2.000
S(2)	0.335$^{6\rightarrow}$			2.008	2.000
Sum.	1.005	1.457	3.057		
Theor.	1.000	1.333	3.000		

Notes: Bond valence sums were calculated with the site-occupancy factors given in Table 4. Calculations were using the equation and constants of Brown (1977), $S = \exp[(R_0 - d_0)/b]$.

This is the peer-reviewed, final accepted version for American Mineralogist, published by the Mineralogical Society of America.
The published version is subject to change. Cite as Authors (Year) Title. American Mineralogist, in press.
DOI: https://doi.org/10.2138/am-2022-8761. http://www.minsocam.org/

TABLE 8. Caluculated X-ray powder diffraction data (*d* in Å) for tetrahedrite-(Ni)

I_{cal}	d_{calc}	*h k l*	I_{cal}	d_{calc}	*h k l*
1.30	7.317	0 1 1	5.80	1.679	2 3 5
3.70	5.174	0 0 2	1.60	1.636	0 2 6
2.70	4.224	1 1 2	1.20	1.597	1 4 5
9.80	**3.659**	**0 2 2**	**20.90**	**1.560**	**2 2 6**
100.00	**2.987**	**2 2 2**	2.30	1.526	1 3 6
9.00	2.766	1 2 3	2.30	1.494	4 4 4
21.20	**2.587**	**0 0 4**	1.60	1.463	3 4 5
8.20	2.439	1 1 4	1.40	1.408	3 3 6
2.60	2.314	0 2 4	3.60	1.293	0 0 8
2.20	2.206	2 3 3	3.20	1.237	3 5 6
2.10	2.112	2 2 4	3.30	1.203	1 3 8
5.60	2.029	1 3 4	4.90	1.187	2 6 6
5.60	1.889	1 2 5	1.40	1.172	2 5 7
41.20	**1.829**	**0 4 4**	1.30	1.157	0 4 8
2.10	1.775	3 3 4	1.70	1.091	4 5 7

*Intensity and d_{hkl} were calculated using the software *VESTA* (Momma and Izumi, 2011) on the basis of the structural model given in Table 4. The five strongest reflections are given in bold.

This is the peer-reviewed, final accepted version for American Mineralogist, published by the Mineralogical Society of America.
The published version is subject to change. Cite as Authors (Year) Title. American Mineralogist, in press.
DOI: https://doi.org/10.2138/am-2022-8761. http://www.minsocam.org/

Figure 1

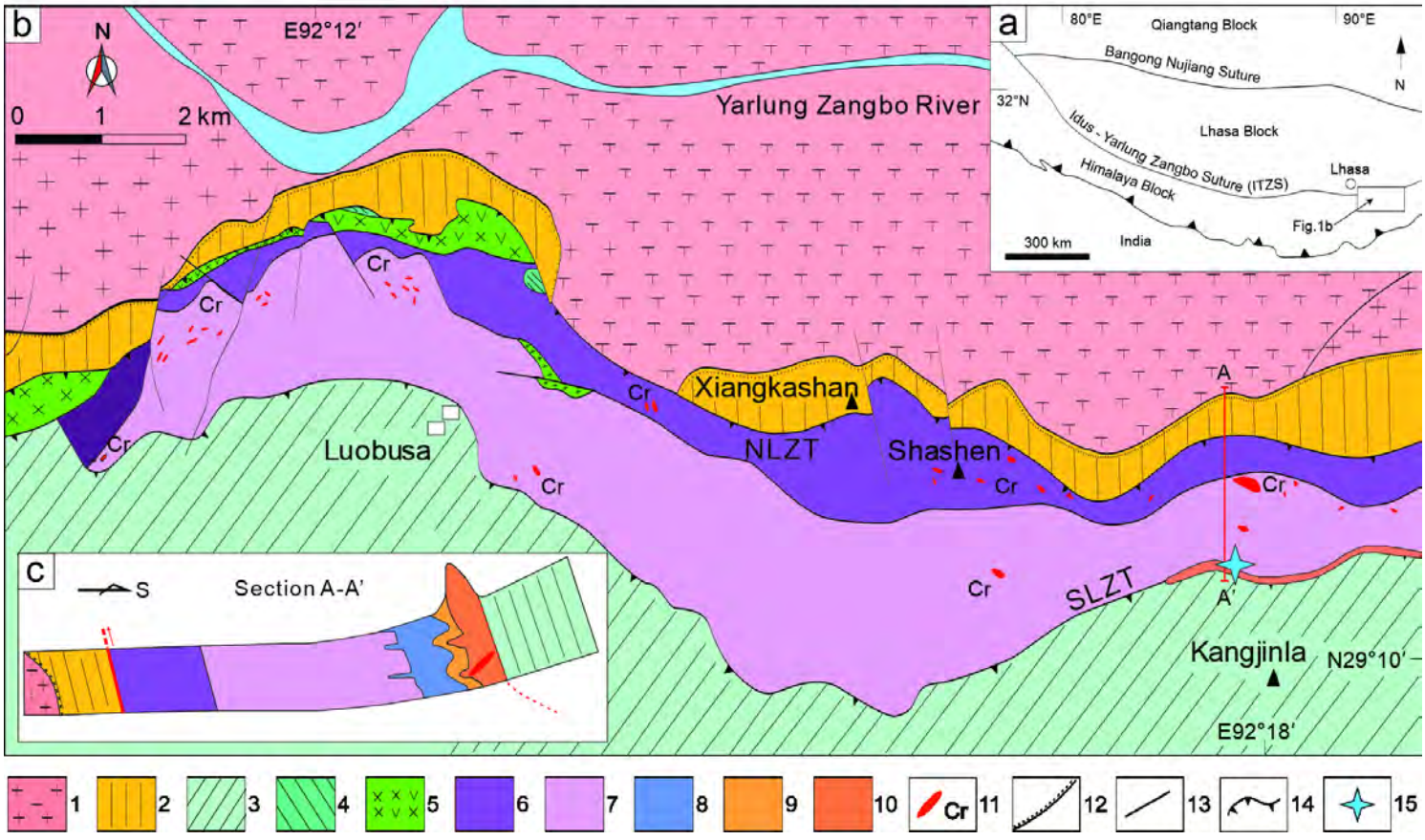

Figure 2

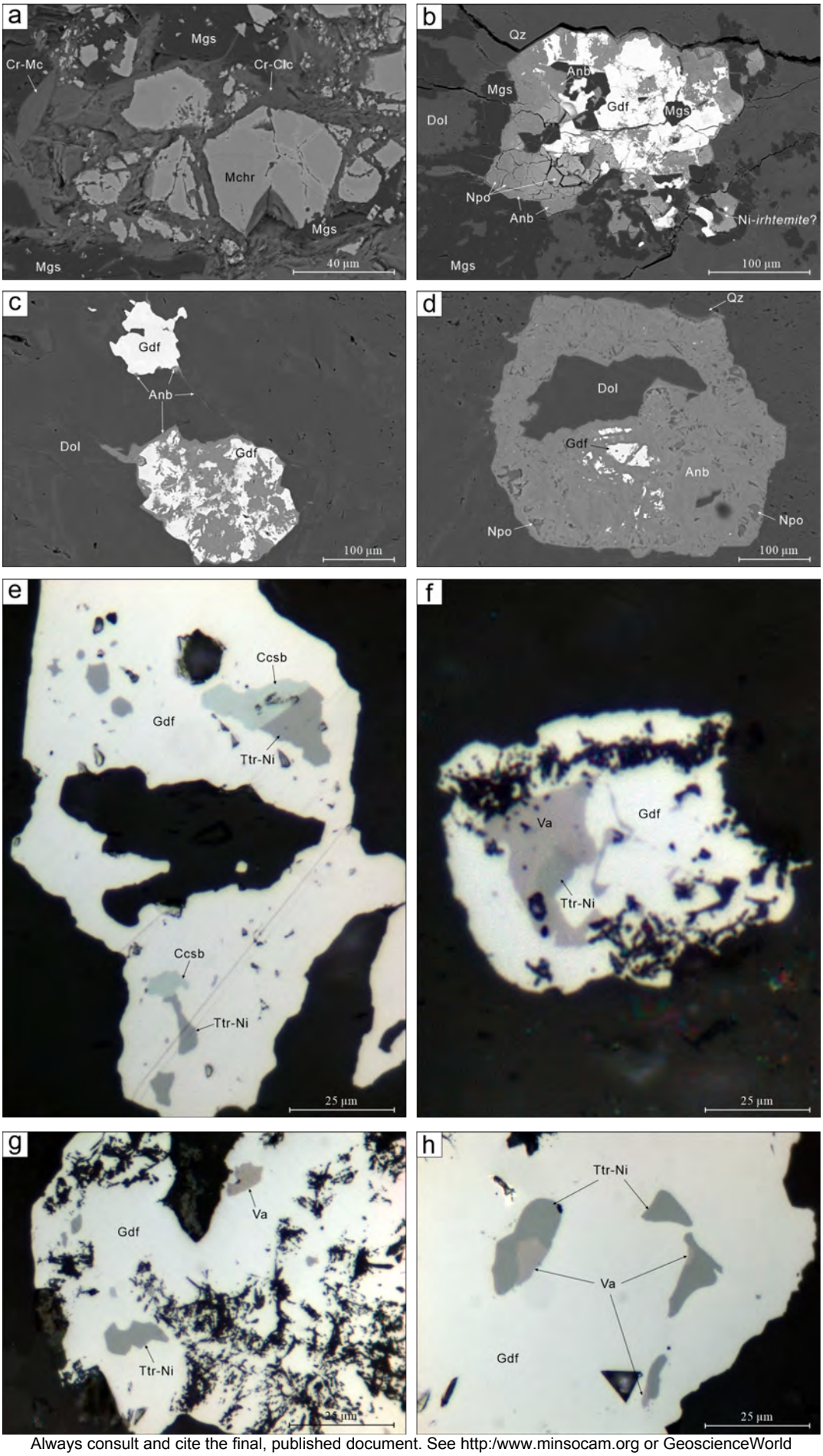

Figure 3

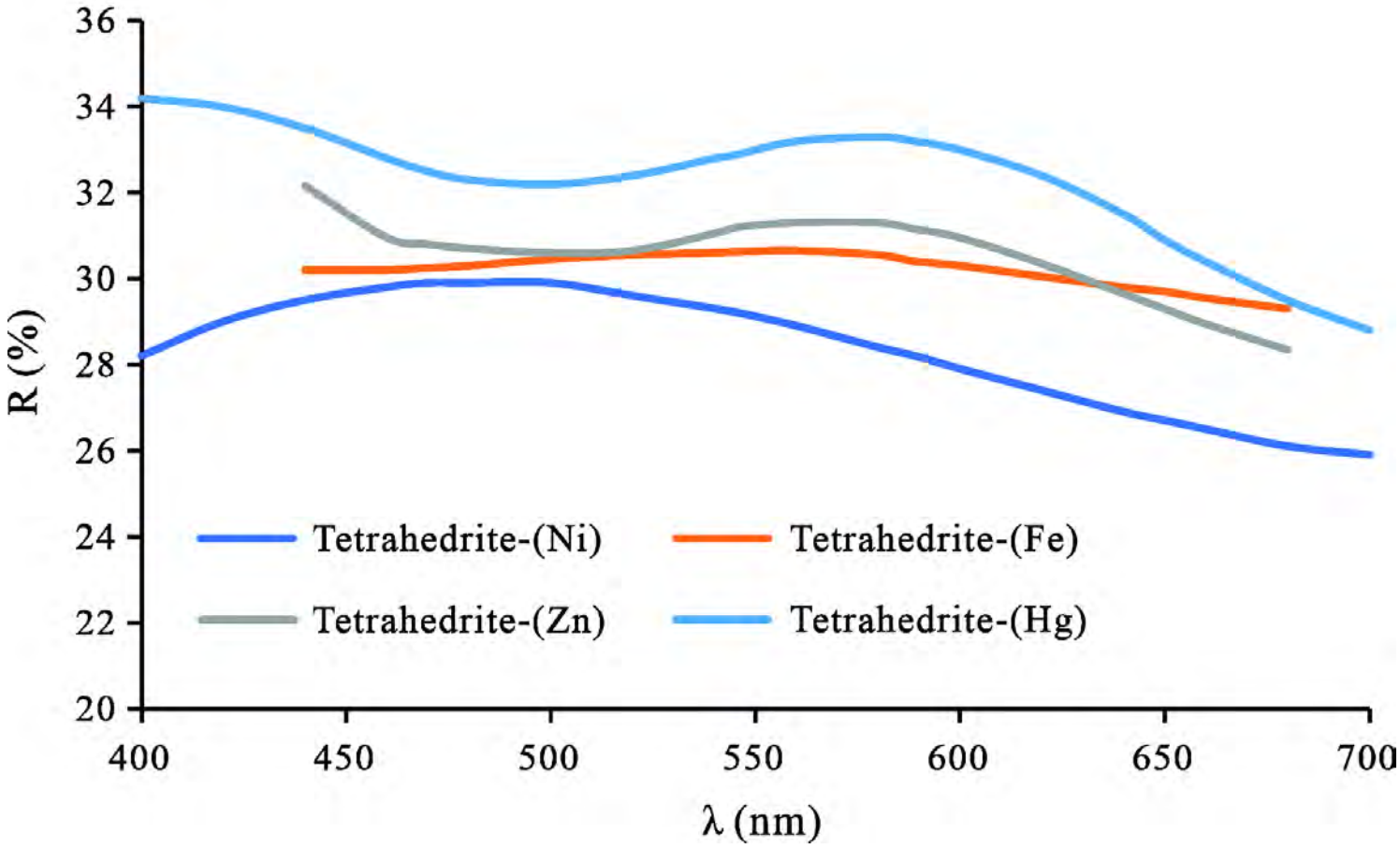

This is the peer-reviewed, final accepted version for American Mineralogist, published by the Mineralogical Society of America.
The published version is subject to change. Cite as Authors (Year) Title. American Mineralogist, in press.
DOI: https://doi.org/10.2138/am-2022-8761. http://www.minsocam.org/

Figure 4

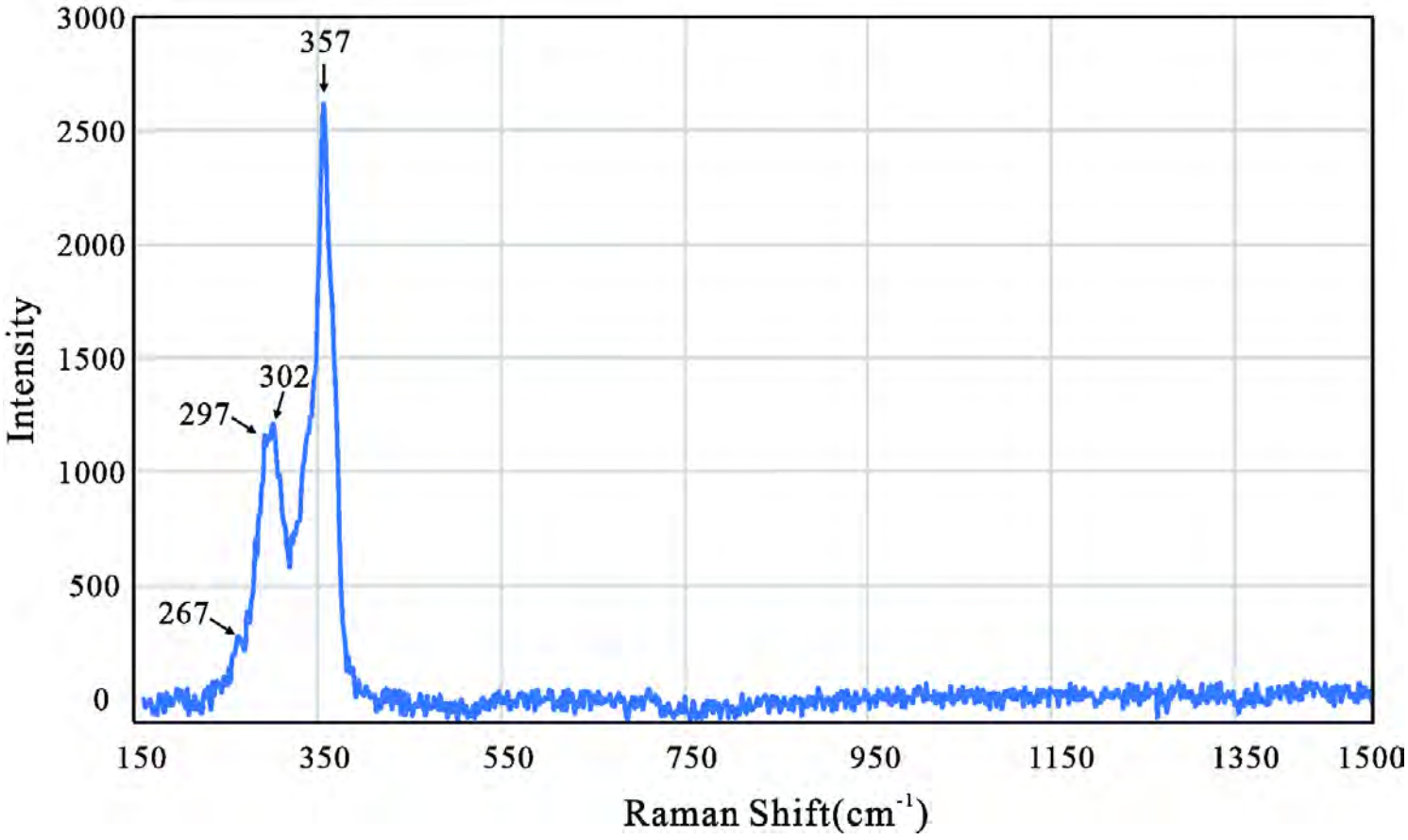

This is the peer-reviewed, final accepted version for American Mineralogist, published by the Mineralogical Society of America.
The published version is subject to change. Cite as Authors (Year) Title. American Mineralogist, in press.
DOI: https://doi.org/10.2138/am-2022-8761. http://www.minsocam.org/

Figure 5

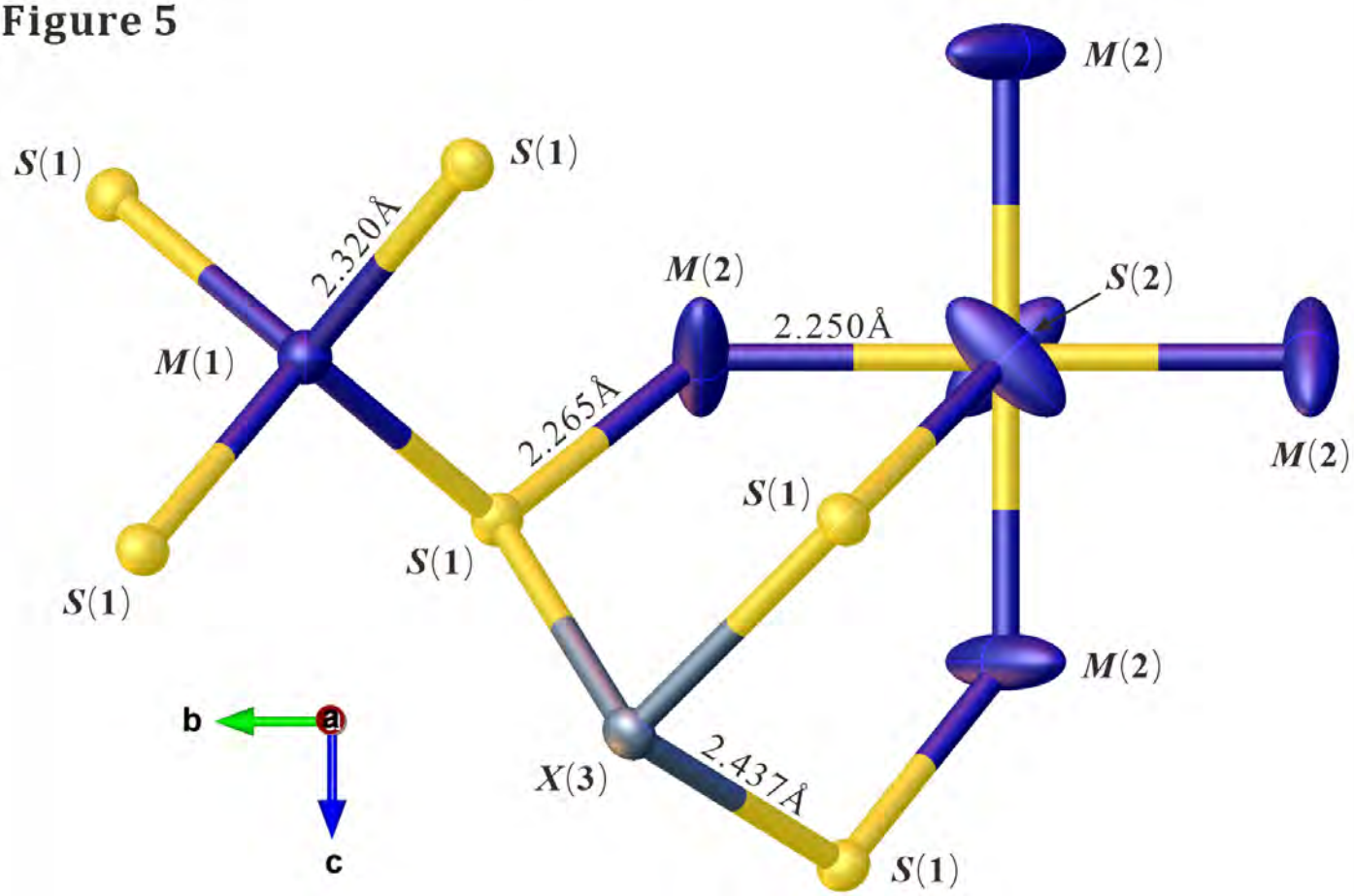

This is the peer-reviewed, final accepted version for American Mineralogist, published by the Mineralogical Society of America.
The published version is subject to change. Cite as Authors (Year) Title. American Mineralogist, in press.
DOI: https://doi.org/10.2138/am-2022-8761. http://www.minsocam.org/

Figure 6